Original Article

The International Journal of
Robotics Research
2025, Vol. 0(0) 1–19
© The Author(s) 2025
Article reuse guidelines:
sagepub.com/journals-permissions
DOI: 10.1177/02783649241310885
journals.sagepub.com/home/ijr
Sage

Expanded quasi-static models to predict the performance of robotic skins on soft cylinders

Jennifer C Case[1,2,3], **Gabrielle Branin**[1], **Ellen Yang**[1],
Stephanie J Woodman[1], **James Gibert**[2] and
Rebecca Kramer-Bottiglio[1]

Abstract

Robotic skins with embedded sensors and actuators are designed to wrap around soft, passive objects to control those objects from their surface. Prior state estimation and control models relied on specific actuator and sensor placement in robotic skins wrapped around soft cylinders, as well as used simplistic assumptions based on geometry and an ideal connection between the robotic skin and underlying structure. Such assumptions limit model fidelity and affect its utility in the design and control of surface-actuated systems. In this work, we relax prior assumptions and present a new quasi-static model with mechanics, controls, state estimation, and kinematic sub-models, or modules, for robotic skins placed around cylindrical structures. The kinematics module is used post-process to analyze the performance of the other three modules. We test the utility of the model on two robotic skin designs and compare the performance against a previous model and physical experiments. We demonstrate that the mechanics, controls, and state estimation modules presented herein outperform the previous model and the mechanics module can be used to predict the behavior of new robotic skin designs. The accuracy of the model increases as the stiffness of the host body material increases. This expanded theory could be utilized to reduce fabrication costs and speed up the design process and could be further extended to include system dynamics and model systems with multiple robotic skins.

Keywords

Robotic skins, soft robots, continuum robots, modeling

Received 17 January 2023; Revised 26 November 2024; Accepted 7 December 2024

1. Introduction

Future missions may require a robot to adapt its morphology and behavior to different tasks or environments. One potential approach to achieve adaptable and modifiable robots is to use robotic skins with embedded actuators that can be applied to the surface of soft, deformable objects to impart motion onto those objects. By applying the skin to different host objects, robots with different functions can be designed on-the-fly (Booth et al., 2018). Such skins have been demonstrated with fluidic (Booth et al., 2018; Campisano et al., 2017; Zhu et al., 2020), cable-driven (Mehringer et al., 2017), jamming (Steltz et al., 2009; Shah et al., 2021, 2023b), and dielectric elastomer actuation (Koo et al., 2008; Guo et al., 2020) for locomotion, wearable devices, manipulation, and medical devices. While these skins have proven useful in myriad applications, sensor data is needed to automate the skins. Sensing skins (Shih et al., 2020; Roberts et al., 2021; Koo et al., 2024) have been manufactured using thin metal (Hwang et al., 2007), carbon nanotubes (Lipomi et al., 2011; O'Neill et al., 2018; Sharma et al., 2023), carbon black (Heng et al., 2021), fluidic (Soter et al., 2019; Shah et al., 2023a), ionic (Chossat et al., 2015), hydrogel (Larson et al., 2016; Yan et al., 2022), conductive threads, yarns, and fabrics (Teyssier et al., 2021; Lv et al., 2022), piezoelectric (Shu et al., 2023), and light (Hughes et al., 2018) sensors.

---

[1]School of Engineering & Applied Science, Yale University, New Haven, CT, USA
[2]School of Mechanical Engineering, Purdue University, West Lafayette, IN, USA
[3]Intelligent Systems Division, National Institute of Standards and Technology, Gaithersburg, MD, USA

Corresponding author:
Rebecca Kramer-Bottiglio, School of Engineering and Applied Science, Yale University, 9 Hillhouse Ave, New Haven, CT 06520, USA.
Email: rebecca.kramer@yale.edu

By including both sensing and actuating elements into robotic skins, they can theoretically turn any compliant body into a soft robot capable of informed actuation via surface manipulation. The development of robotic skins with both sensing and actuating capabilities is still in the preliminary stages. Existing skins use sensor inputs to measure pressure in fluidic chambers (Campisano et al., 2017) or to measure strain along actuators (Booth et al., 2018; Case et al., 2018, 2019).

We focus specifically on the type of robotic skin first presented by Booth et al. (2018) that has axially-contracting actuators and strain sensors on a planar substrate. For simplicity, when we refer to "robotic skin" throughout the remainder of the paper, we are referencing this specific subtype of robotic skins. Prior work presented mechanics, controls, and state estimation models for a robotic skin design wrapped around a soft cylindrical structure, in which four strain sensors and axially-contracting actuators are evenly spaced parallel to the neutral axis (shown in the top row of Figure 1) (Booth et al., 2018; Case et al., 2018, 2019). This skin design enables cylinder bending and was shown to be valuable for various applications, such as locomotion and grasping (Booth et al., 2018). In previous work, we demonstrated state and stiffness estimation of soft cylinders using geometric constraints based on the robotic skin design and a simple quasi-static mechanics model, which ignored inertial effects (Case et al., 2018). We then expanded on the mechanics model and added a quasi-static feedforward control model that predicted actuator inputs given a desired state of the cylinder (Case et al., 2019).

While the previous works (Booth et al., 2018; Case et al., 2018, 2019) have demonstrated progress toward modeling robotic skins, they restricted the design of the skins to a single configuration. We recently highlighted the benefits of alternative skin designs by demonstrating a walking robot using twisting skins (Case et al., 2020), where the sensors and actuators spiraled around the outside of a cylindrical structure (shown in the bottom row of Figure 1). In addition to limiting the skin design, the previous models made several assumptions about the behavior of the system: (1) the skin conforms perfectly to the underlying structure, (2) the only meaningful forces from the skin are from the actuators, which also means that gravity is considered negligible, and (3) the axial length of the structure is incompressible, a necessary condition for geometric formulations in the model.

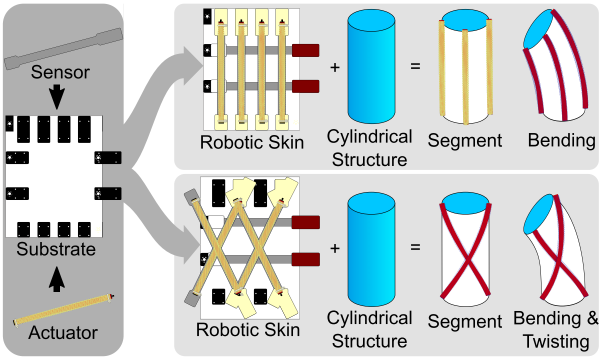

Figure 1. Diagram showing the difference between robotic skins with strain sensors and actuators placed parallel to the neutral axis and strain sensors and actuators placed on an angle such that they form helixes around the structure.

The goal of this work is to expand the mechanics, controls, state estimation, and kinematic models that can predict the performance of robotic skins by loosening the constraints on component placement. Specifically, these models apply to robotic skins with axially contracting actuators and strain sensors that are wrapped around cylindrical structures. The expanded model presented herein not only allows generalized placement of sensors and actuators, but also (1) adds a spring-like interface between the robotic skin and the host cylindrical structure, (2) accounts for sensor and gravitational forces, and (3) allows the axial length of the structure to compress under load. The model is quasi-static and therefore ignores the inertial effects of the system. We demonstrate that the expanded model outperforms previously published models. Additionally, we demonstrate how the mechanics sub-model, or module, can be used to predict the behavior of an alternative skin design with helically wrapped actuators, which highlights the benefit of using these models during the design phase of robotic skins.

The paper is organized as follows. The Review of the Previous Model section provides an overview of the previous model for robotic skins, contextualized within existing models for continuum robots. The Expanded Model section explains the new, expanded model. In the Model Validation section, we discuss the model validation including the designs of the skins used for physical experimentation, the experiments that were conducted, and the results of our analyses of the experiments. Finally, we conclude the paper and discuss future work.

2. Review of the previous model

In this section, we provide a brief overview of the previous model that this paper extends. The prior model limited the sensor and actuator placement to a single configuration with four actuators and sensors spaced evenly around a cylinder running parallel to the neutral axis, shown in Figure 2, which enables the models to take advantage of the

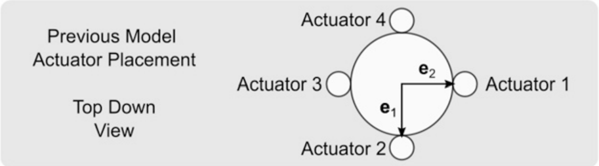

Figure 2. Diagram showing actuator placement for the previous models (Case et al., 2019). Recall that these models assumed a pre-determined actuator and sensor placement. Sensors are assumed to be in-line with the actuators.

geometrical limitations and assumes quasi-static behavior of the system, thus neglecting inertial effects. The previous model (Case et al., 2019) consists of three sub-models, which will be referred to as modules: (1) a mechanics module that takes pressures from the actuators and predicts the equilibrium state of the system; (2) a controls module that inverts the mechanics module, taking the state of the system and estimating the pressures required from the actuators; and (3) a state estimation module that takes the sensor length measurements and estimates the state of the system.

In the previous model, the state ($\mathbf{q}_{\text{prev}}$) of the system is defined as

$$\mathbf{q}_{\text{prev}} = \{\kappa_{\mathbf{e}_1}, \kappa_{\mathbf{e}_2}\}, \tag{1}$$

where $\kappa_{\mathbf{e}_i}$ is curvature with respect to the $\mathbf{e}_i$-axis.

3. Expanded model

The model presented herein generalizes the previous model by expanding sensor and actuator placement compared to previous designs. For these models, we make several assumptions (i.e., the robotic skin is placed on a cylindrical structure and the sensors and actuators run from one end of the cylinder to the other) that enable us to build upon existing models from the literature on continuum robots (Camarillo et al., 2008; Webster and Jones, 2010; Renda et al., 2012; Rucker and Webster, 2014; Burgner-Kahrs et al., 2015; Renda et al., 2016; Faulkner and Dirven, 2017; Zhang et al., 2022; Russo et al., 2023; Tummers et al., 2023; Almanzor et al., 2023; Armanini et al., 2023; Della Santina et al., 2023). This work has commonalities with continuum robots that have generalized tendon placement (Rucker and Webster, 2014), which uses models that assume slender Cosserat rods ($l/r > 5$, where l and r are the length and radius of the rod, respectively) for the backbone. Because the cylindrical structures used in this work were not slender (l/r = 3.3), we used linear solid mechanics since we found that this method provides a good estimation given the achievable deformations of the skin-structure system. Modeling of robotic skins could be improved further by incorporating alternative modeling techniques, such as nonlinear material models, continuum mechanics, and other robotic skin models (Zhu et al., 2020).

The theory behind the model is presented in two sections: (1) segment modeling, which explains the underlying assumed behavior for the components in a segment as shown in Figure 3, and (2) model modules, which explains the mechanics, controls, state estimation, and kinematics modules.

3.1. Segment modeling

A segment consists of a cylindrical structure with rigid end caps on the ends wrapped with a robotic skin, which is made up of a substrate, sensors, and actuators. To facilitate the use of homogeneous transformations, coordinate systems were applied along the length of the segment's underlying structure to easily reference the cylindrical structure and rigid end caps, shown in Figure 4(a).

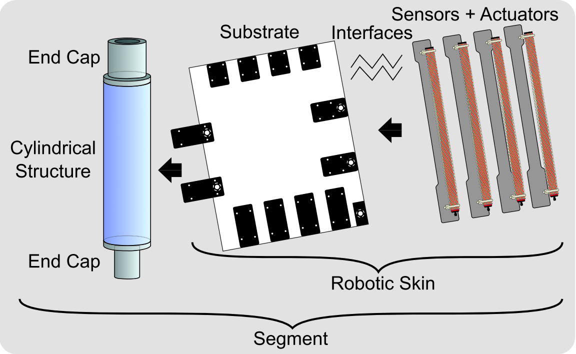

Figure 3. Graphics explaining the various components of the physical system.

3.1.1. Cylindrical structure. One of the most important aspects of the cylindrical structure is its state. For the deformation of the structure, we assume piece-wise constant curvature by assuming no external forces on the system and that the structure is compressible along the neutral axis. The compressibility of the cylindrical structure will be referenced with a "C" in the Model Validation section. To allow for more generalized placement of the sensors and actuators, we have included twisting alongside bending and compression in our state definition ($\mathbf{q}$),

$$\mathbf{q} = \{\kappa, \phi, \lambda, \alpha_{max}\}^T, \tag{2a}$$

$$= \{\kappa_{\mathbf{e}_1}, \kappa_{\mathbf{e}_2}, \lambda, \alpha_{max}\}^T, \tag{2b}$$

$$\kappa = \sqrt{\kappa_{\mathbf{e}_1}^2 + \kappa_{\mathbf{e}_2}^2},$$

$$\phi = \tan^{-1}(\kappa_{\mathbf{e}_1}/\kappa_{\mathbf{e}_2}),$$

where κ is the curvature, ϕ is the angular offset of the curvature, $\kappa_{\mathbf{e}_i}$ is the curvature with respect to the $\mathbf{e}_i$-axis, λ is the stretch along the centerline of the cylindrical structure (which relates to the compression of the structure along the centerline), and α_{max} is the maximum twist of the structure. This angular twist at any arbitrary location along the uncompressed length of the cylindrical structure (s) is found using the following

$$\alpha = \alpha_{max} s / l_{cyl}, \tag{3}$$

where l_{cyl} is the length of the cylindrical structure. A visual representation of the state is shown in Figure 4(b).

The state was integrated into a homogeneous transformation that was adapted from Webster and Jones (2010) to include twist,

$${}^{1}\mathbf{T}_2 = \begin{bmatrix} r_{11} & r_{12} & s_\theta c_{\alpha+\phi} & -\kappa^{-1} v_\theta c_{\alpha+\phi} \\ r_{21} & r_{22} & s_\theta s_{\alpha+\phi} & -\kappa^{-1} v_\theta s_{\alpha+\phi} \\ -c_\phi s_\theta & -s_\phi s_\theta & c_\theta & \kappa^{-1} s_\theta \\ 0 & 0 & 0 & 1 \end{bmatrix}, \tag{4}$$

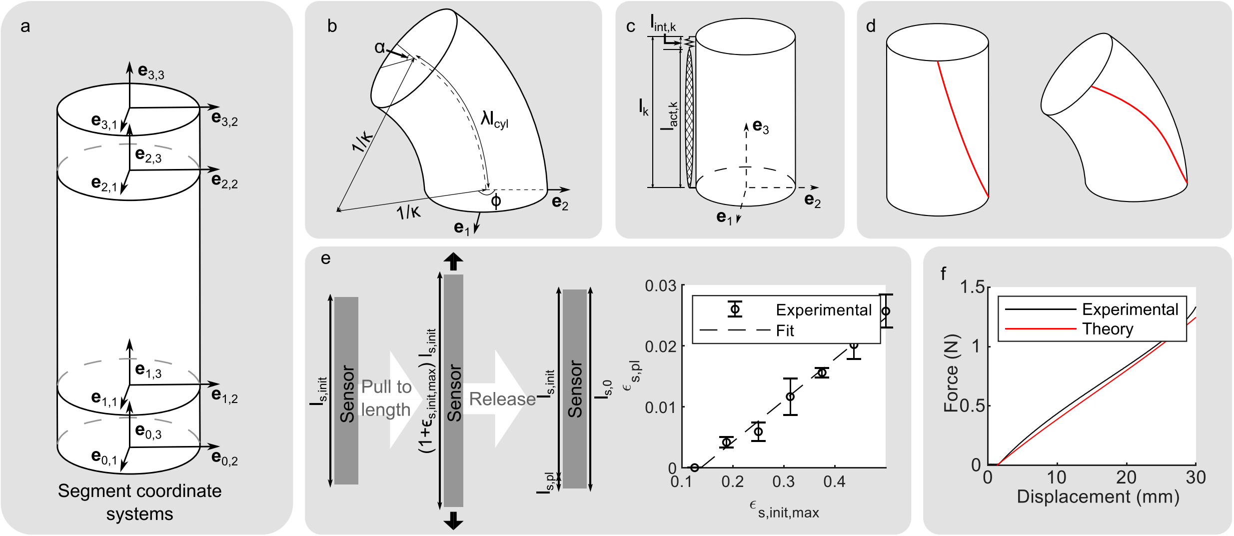

Figure 4. (a) Representation of the coordinate frames placed along the segment. (b) General model showing the state of the system. (c) Example of the skin-structure interface. (d) Visual representation of how the sensor and actuator position changes from the reference configuration to the deformed configuration. (e) The relationship between the plastic deformation in a strain sensor and the initial sensor length. The error bars represent one standard deviation. (f) Experimental force versus displacement sensor results compared to the theoretical model.

$$r_{11} = c_\phi v_\theta c_{\alpha+\phi} + c_\alpha,\; r_{12} = c_\phi v_\theta s_{\alpha+\phi} - s_\alpha c_\theta$$

$$r_{21} = c_\phi v_\theta s_{\alpha+\phi} + s_\alpha,\; r_{22} = -c_\phi v_\theta c_{\alpha+\phi} + c_\alpha c_\theta$$

where ${}^{1}\mathbf{T}_2$ is the homogeneous transformation describing the cylindrical structure deformation, and $c_x = \cos(x)$, $c_{x+y} = \cos(x+y)$, $s_x = \sin(x)$, $s_{x+y} = \sin(x+y)$, $v_x = c_x - 1$, and $\theta = \kappa\lambda s$ is the angle of curvature.

3.1.2. End caps. Since the end caps are rigid and are assumed to remain undeformed as the skin actuates, the only notable parameter is the length of the end cap (l_{cap}). The homogeneous transformation to describe the end cap is given by

$$ {}^{0}\mathbf{T}_1 = {}^{2}\mathbf{T}_3 = \begin{bmatrix} 1 & 0 & 0 & 0 \\ 0 & 1 & 0 & 0 \\ 0 & 0 & 1 & l_{cap} \\ 0 & 0 & 0 & 1 \end{bmatrix}, \tag{5}$$

where ${}^{0}\mathbf{T}_1$ and ${}^{2}\mathbf{T}_3$ refers to the end cap attached to the bottom and top of the cylindrical structure, respectively.

3.1.3. Robotic skin. The robotic skin generates forces from actuators, sensors, and the substrate of the skin itself. For simplicity, the robotic skins used in this work were designed such that forces generated by the substrate are assumed to be negligible, which means that the substrate is assumed not to stretch along the neutral axis of the cylindrical structure when placed on the structure. Thus, the model assumes all the relevant forces come from the sensors and actuators through an interface that represents the imperfect connection between the skin and the underlying structure. We have included some initial strategies surrounding the inclusion of forces from the substrate in the Supplemental Materials (Section S1) although these strategies were not utilized in the model presented in this paper.

3.1.4. Interface. To account for the fact that forces from sensors and actuators cause internal deformations in the robotic skins at their attachment points, a virtual interface element, which is modeled as a linear spring, was introduced between the ideal representation of the body and the model of the actuator. An example of this skin-structure interface connected to an actuator is shown in Figure 4(c). The interface model feature will be referenced with a "I" in the Model Validation section.

The force applied to the interface (F_{int}) is given by

$$F_{int} = F_a + F_s, \tag{6}$$

where F_a and F_s are the forces from the actuator and sensor attached to the interface, and the subscript $(\cdot)_{int}$ indicates that the term relates to the interface. Note, here, that we used unbolded font to indicate the magnitude of the force (e.g., $F_{int} = \|\mathbf{F}_{int}\|$) for simplicity. The direction of the force will be discussed later.

Because the interface is modeled with a linear spring element, the length of the interface (l_{int}) can be found using Hooke's law,

$$l_{int} = k_{int}^{-1} F_{int}, \tag{7}$$

where k_{int} is the stiffness of the interface. We define this variable empirically in the work when testing our robotic skins.

Since the interface attaches to both actuators and sensors, we provide the model description of how actuators and sensors are placed onto the skin here. It is assumed that the actuators and sensors wrap around the cylindrical structure when the skin is applied, and, thus, the actuator and sensor paths were described with space curves,

$$\mathbf{R}(s) = \{r\cos(\beta_0 s + \beta_1), r\sin(\beta_0 s + \beta_1), s\}^T, \quad s \in [0, l_{cyl}], \tag{8}$$

where β_i for $i = 0, 1$ are the attachment constants defining the placement of the actuator or sensor along the circumference of the cylindrical structure. An example of what these space curves look like is shown in Figure 4(d).

This spatial description of the sensors and actuators can then be used to determine the force vector experienced on the interface using

$$\mathbf{F}_{int} = -F_{int}\frac{\mathbf{R}'(l_{cyl})}{\|\mathbf{R}'(l_{cyl})\|}. \tag{9}$$

where $(\cdot)' = \partial/\partial s$. Equation (9) assumes that the force is tangential to the direction of the space curve in the undeformed configuration at the top of the cylindrical structure.

3.1.5. Actuator. For our actuator model, we utilize an empirically-derived polynomial model (Case et al., 2019) given as

$$F_{a,k} = c_0 + c_1 P_{a,k} + c_2 l_{a,k} + c_3 P_{a,k} l_{a,k} + c_4 l_{a,k}^2 \tag{10}$$

where $F_{a,k}$, $P_{a,k}$, and $l_{a,k}$ are the force, pressure, and length of the kth actuator, respectively, $(\cdot)_a$ indicates that the term (e.g., force, pressure, length) relates to the actuators, and c_i for $i = 0, 1, \ldots, 4$ are constants empirically-derived through linear regression via the normal equation for a given actuator. This empirically derived model provides accurate force estimates for the actuators. Further discussion comparing empirical and theoretical models of the actuators is provided in the Supplemental Materials (Section S2).

3.1.6. Sensor. Previous models of robotic skins neglected forces from the elastomer-graphite composite sensors used in the construction of the skins. However, these sensors can generate forces large enough to affect the underlying structure and, thus, should be included in models of the skins. The forces from the sensors will be referenced with an "F" in the Model Validation section. To model the sensors, we consider both the forces they generate as well as the plastic deformation they experience through undergoing axial strain. An understanding of the sensor behavior is required to select an appropriate sensor length for the skins.

To understand plastic deformation, a sensor with an initial length of 80 mm was cyclically strained in a materials testing machine (Instron 3345[1]) to several deflections (10–40 mm at 5 mm intervals) at a rate of 50 mm/min. The sensor was cycled seven times at each deflection before progressing to the next deflection. The first two cycles of the seven were discarded to eliminate response due to the Mullin's effect (Mullins, 1948). During these cycles, the sensor's force response plateaued as it approached the initially designed sensor length (see the Supplemental Materials (Section S3) indicating plastic deformation. The strain of the initially designed sensor length can be linearly mapped to the strain of plastic deformation, as shown in Figure 4(e), via

$$l_{s,pl} = \epsilon_{s,pl} l_{s,init}, \tag{11a}$$

$$\epsilon_{s,pl} = \begin{cases} d_0 \epsilon_{s,init,max} + d_1 & \epsilon_{s,init,max} > -d_1/d_0 \\ 0 & \epsilon_{s,init,max} \leq -d_1/d_0 \end{cases}, \tag{11b}$$

where $l_{s,pl}$ is the change in length due to plastic deformation, $l_{s,init}$ is the initial designed sensor length, $\epsilon_{s,init,max}$ is the maximum strain of the sensor taken from the initial sensor length, $(\cdot)_s$ indicates that the term relates to the sensors, and d_i for $i = 0, 1$ are linear fit constants. Figure 4(e) visually shows the lengths related to sensors and the relationship between $\epsilon_{s,init,max}$ and $\epsilon_{s,pl}$. Using the experimental data, the constants were found to be $d_0 = 0.0679$ and $d_1 = -0.0093$.

To capture the force-displacement behavior of these sensors, an empirically-derived Ogden material model (Ogden and Ogden, 2003) was used alongside the empirically derived model to capture the plastic deformation seen in our sensors. The force-displacement model is captured by

$$F_{s,j} = \begin{cases} wt\lambda_s^{-2v_s} \sum_{i=1}^{N} \mu_i f(\lambda_s, \gamma_i) & \text{if } l_s \geq l_{s,0} \\ 0 & \text{if } l_s < l_{s,0} \end{cases}, \tag{12a}$$

$$f(\lambda_s, \gamma_i) = \lambda_s^{\gamma_i - 1} - \frac{1}{3}(2\lambda_s^{-(1+\gamma_i)/2} + \lambda_s^{1+\gamma_i})\lambda_s^{-2} \tag{12b}$$

$$\lambda_s = \frac{l_s}{l_{s,0}}, \tag{12c}$$

$$l_{s,0} = l_{s,init} + l_{s,plas}, \tag{12d}$$

where $F_{s,j}$ is the jth sensor force due to strain, w is the sensor width, t is the sensor thickness, N is the number of terms for the Ogden model, v_s is the Poisson ratio of the sensor material ($v_s = 0.5$ with assumed incompressibility), l_s is the strained sensor length, and $l_{s,0}$ is the unstrained sensor length after it has been pre-strained to account for plastic deformation. To determine the Ogden model, the model was fit to experimental data from a sensor that was strained 60 mm/min for 12 cycles with a materials testing machine (Instron 3345[1]). A three parameter ($N = 3$) Ogden model was used with a fit of $\mu_1 = 2960$, $\mu_2 = 50200$, $\mu_3 = 75700$, $\gamma_1 = 7.88$, $\gamma_2 = 0.689$, and $\gamma_3 = 0.689$. In determining this Ogden model, the plastic deformation was removed from the sensor response.

To test how well the new sensor model captured the plastic deformation of the sensors, the model was compared to the same experimental data used to determine the Ogden model. This same sensor was used because we have previously shown high repeatability in the sensor response

(White et al., 2017) and this sensor was different than the one we had used to determine the plastic deformation. There was good agreement in the prediction of the plastic deformation between the model and experimental data, shown in Figure 4(f). Thus, this model was a valid approximation of the force from the sensors.

3.2. Model modules

With a better understanding of how each of the components of the segments fit together, we can explain how to use these components to achieve an improved mechanics, controls, and state estimation modules. An overview of the functional modules is given in Figure 5. There are four functionality modules included in this theory: (1) mechanics, (2) controls, (3) state estimation, and (4) kinematics.

3.2.1. Mechanics module.

The mechanics module provides a mapping between forces and moments experienced by the segment to the state of the segment using our homogeneous transformation from equation (4). We discuss forces from the sensors and actuators and the weight of the segment before discussing how they are used to determine the state of the system.

As force from an actuator or sensor is applied to the interface, the lengths of the interface, actuator, and sensor all change, which in turn affects the force from the actuator and/or sensor. We can calculate the total length of the interface and the attached actuator and/or sensor, l_k, via

$$l_k = \int_0^{l_{cyl}} \|\mathbf{r}_k'(s)\| ds, \tag{13a}$$

$$\mathbf{r}(s) = {}^1\mathbf{T}_2 \begin{Bmatrix} \mathbf{R}(s) \\ 0 \end{Bmatrix}, \tag{13b}$$

where $\mathbf{r}(s)$ is the deformed path of the interface and sensor and/or actuator. Figure 4(d) shows an illustration of how the path changes from its undeformed configuration.

Thus, the length of the attached sensor and/or actuator is given by

$$l_{sen,k} = l_{act,k} = l_k - l_{int,k}. \tag{14}$$

From these equations, we can see that optimization is required to adjust the sensor and actuator lengths such that the total path length is correct, as shown in Figure 5.

The weight of the segment is calculated using a point mass at the center of the segment. Accounting for the weight of the segment enables more accurate estimations since the material can bend under its own weight. The forces from gravity (i.e., the weight of the segment) will be referenced with a "G" in the Model Validation section. The force vector from the weight is described using

$$\mathbf{W} = \mathbf{w}mg, \tag{15}$$

where m is the mass of the segment, g is the gravitational constant, $\mathbf{w}$ is a unit vector describing the direction of gravity in the global coordinate frame. For this work, $\mathbf{w} = \{0,0,-1\}^T$. The moment arm for the weight, which spans from the origin of the $\mathbf{e}_1$-coordinate frame to the center of

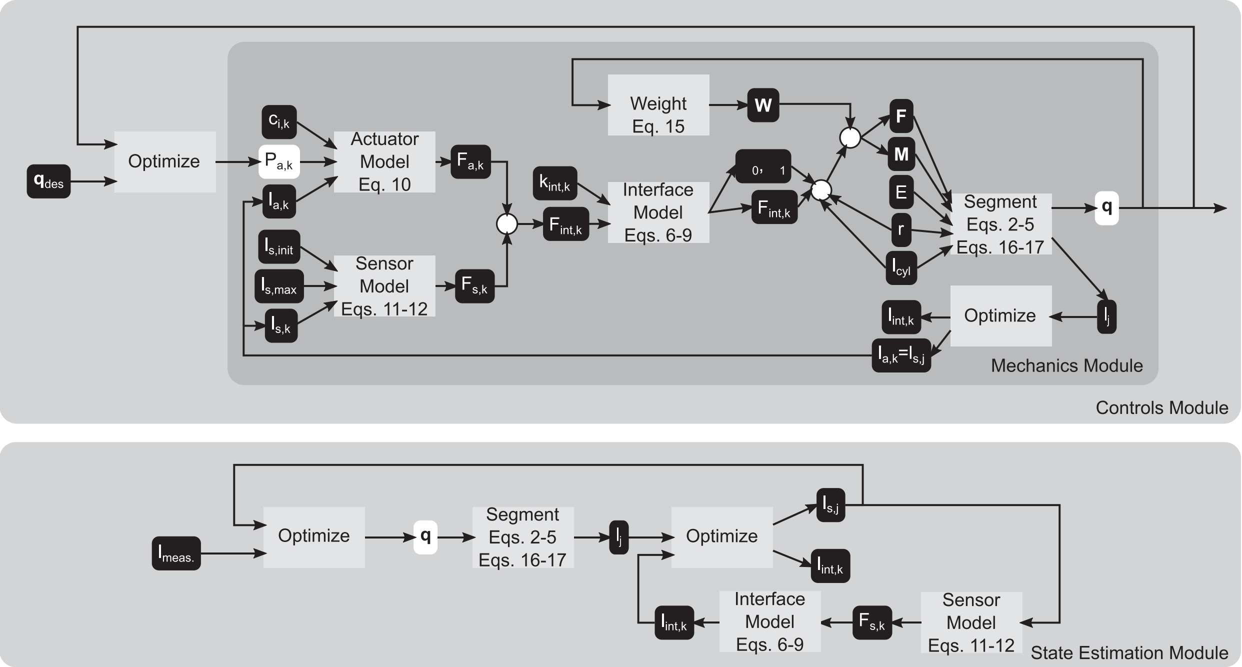

Figure 5. An overview of the modules and how they interact with the different component sub-models. This diagram points to relevant sections of the paper for each component.

mass of the segment, is given by $\mathbf{d}_w$ and is dependent on the state of the segment.

With the forces defined, we can calculate the force and moment equations on the segment with

$$\mathbf{F} = -mg\mathbf{w} - \sum_{k=0}^{n-1} \mathbf{F}_{int,k}, \tag{16a}$$

$$\mathbf{M} = -mg(\mathbf{d}_w \times \mathbf{w}) - \sum_{k=0}^{n-1} (\mathbf{d}_{int,k} \times \mathbf{F}_{int,k}), \tag{16b}$$

where $\mathbf{F}$ is the force on the segment, $\mathbf{M}$ is the moment on the segment, n is the number of interfaces, and $\mathbf{d}_{int,k}$ is the moment arm to the kth interface.

Using these forces and moments, the mapping to the state can be described as

$$\kappa_{\mathbf{e}_1} = \frac{1}{K_b}\mathbf{M} \cdot \mathbf{e}_2, \tag{17a}$$

$$\kappa_{\mathbf{e}_2} = -\frac{1}{K_b}\mathbf{M} \cdot \mathbf{e}_1, \tag{17b}$$

$$\lambda = 1 - \frac{1}{K_a}\mathbf{F} \cdot \mathbf{e}_3, \tag{17c}$$

$$\alpha = -\frac{1}{K_t}\mathbf{M} \cdot \mathbf{e}_3, \tag{17d}$$

where K_b is bending stiffness ($K_b = EI$, where E is elastic modulus and I is second moment of inertia), K_a is axial stiffness ($K_a = EA$ where A is the cross-sectional area), and K_t is torsional stiffness ($K_t = EI/(2(1 + v))$, where v is Poisson's ratio).

3.2.2. Controls module. The controls module is a feedforward model that inverts the mechanics module taking a desired state as input and providing pressures in the actuator as outputs. Integrating a feedforward model into the control of continuum segments has previously been shown to be beneficial (Case et al., 2019). The previous model's controls module was able to directly invert the mechanics module. However, for this expanded model where actuators can be placed anywhere, no analytical inversion is possible. Therefore, a numerical solver was wrapped around the mechanics module to optimize pressure in the actuators, shown in Figure 5. There are physical boundaries around the pressures ($0 \leq P_{act} \leq 172$ kPa) which limit the achievable deformation. If a desired state is not achievable, the optimization minimizes the error in the state and provides both the pressures in the actuators as well as the state achieved by the segment. This controls module is not currently optimized for use in real-time applications.

3.2.3. State estimation module. To estimate the state of the system, there are no direct analytical models due to the generalized placement of the sensors. Instead, we take a numerical approach and optimize the state given the length measurements from the sensors (l_{meas}), shown in Figure 5. The state of the system is adjusted until the model's sensor lengths match the measured sensor lengths.

3.2.4. Kinematics module. To track points from the reference to the deformed locations, we can use our homogeneous transformations from equations (4) and (5). If the tracked point is at the end of the top end cap, we used the following

$$\mathbf{p}_{i,\,model} = {}^{0}\mathbf{T}_3\mathbf{p}_{i,\,reference} \tag{18}$$

where $\mathbf{p}_{i,model}$ is the deformed point obtained by the model, $\mathbf{p}_{i,reference} = \{x,y,0,1\}^T$ is some point in the reference configuration along the top plane of the top end cap, and ${}^{0}\mathbf{T}_3 = {}^{0}\mathbf{T}_1{}^{1}\mathbf{T}_2{}^{2}\mathbf{T}_3$. If the point is on the cylindrical structure, the following should be used,

$$\mathbf{p}_{i,\,model} = {}^{0}\mathbf{T}_2\mathbf{p}_{i,\,reference}, \tag{19}$$

where the appropriate value of s is used with equations (3) and (4) and $\mathbf{p}_{i,reference} = \{x,y,0,1\}^T$ is the point in the reference configuration.

4. Model Validation

To validate the model, we compare the performance of the mechanics, controls, and state estimation modules against the previous model using the skin design required for the previous model, shown in Figure 6(a) and referred to as a Parallel Skin. We additionally show that the mechanics model can describe the behavior of alternative skins by using the skin shown in Figure 6(b), which is referred to as a Twisting Skin. Two of each type of skin were made to ensure the models worked across skins of the same type and each skin is identified with a number. The fabrication and characterization of the skins and the cylindrical structures are provided in previous publications (Booth et al., 2018; Case et al., 2019, 2020) and in the Supplemental Materials (Section S4).

For our experiments, we used both a motion capture setup and a top-down camera setup to track the position of a segment comprising of either parallel or twisting skins and compare it against the predicted model performances using both our prior model and new extended model. Figure 7 outlines the experiments and more details of the experiments are provided in the Supplemental Materials (Section S5). The parallel skins were placed on all three cylindrical structures: EcoFlex 00–50 (Shore Hardness: 00–50, Smooth-On, Inc.), Dragon Skin 10 (Shore Hardness: 10A, Smooth-On, Inc.), and Smooth-Sil 936 (Shore Hardness: 36A, Smooth-On, Inc.). The twisting skins were placed on the two softest structures: EcoFlex 00–50 and Dragon Skin 10. With the experiments, we completed four studies, outlined in Figure 8, to evaluate the fidelity of each of our improved models.

4.1. Evaluating the performance of the mechanics module for parallel skins

To study the performance of the mechanics module on parallel skins, we considered how the introduction of our new model features (i.e., compressibility, sensor forces, gravitational forces, and skin-structure interfaces) affected the module and how well it could predict complex motion.

4.1.1. Introduction of model features. To understand how model features affected the performance of the module, we performed a full factorial study, shown in Table 1, which compares the effects of different feature combinations against the prior model and physical experimentation (specifically the motion tracking experiments). To simplify the description of the models, the first letters of the model features are used to denote a specific model combination (e.g., C = **C**ompressibility, G = **G**ravity, F = Sensor **F**orce, and I = **I**nterface). For four of the eight model combinations examined in this full factorial study (C/I, C/G/I, C/F/I, and C/G/F/I, as shown in Table 1), an interface spring is needed. Table 2 provides the skin-structure interface spring constants for the combinations described in Table 1 for the Parallel Skin. These spring constants were determined through gradient descent optimization to minimize the normalized error between the model combination and the tracked points given by

$$err = \frac{1}{N_p l_{max}} \sum_{i=1}^{N_p} \|\mathbf{p}_{i,\,model} - \mathbf{p}_{i,\,track}\|, \qquad (20)$$

where err is the normalized averaged distance error between the modeled and tracked points at the top of the segment, N_p is the number of visible tracked points, $\mathbf{p}_{track}$ is the position of the tracked point, $\mathbf{p}_{model}$ is the position of that point according to the model combination, and l_{max} is the maximum travel length for each cylindrical structure, which is calculated by examining the maximum distance traveled by each tracked point on the segment. The maximum length traveled was found to be 78, 67, and 49 mm for EcoFlex 00–50, Dragon Skin 10, and Smooth-Sil 936 with Parallel Skin 1, respectively. For the full factorial study, this error was calculated in two ways: (1) for each pressure individually, and (2) across all the measured pressures.

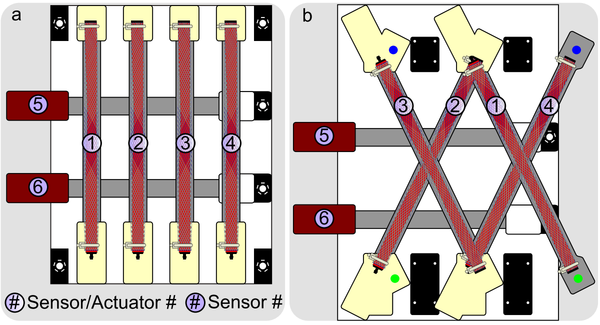

Figure 6. Basic layout for the (a) parallel skins and (b) twisting skins. The actuators and sensors are labeled for reference. The twisting skin is shown flattened, but is circular in reality with the blue dots and green dots representing the same locations.

First, we demonstrate that the extended mechanics module is better able to match the response of the physical system than our previous mechanics module. For this analysis, we consider two of the model combinations described in Table 1: (1) the C feature, which only includes compressibility, and (2) the C/G/F/I combination, which

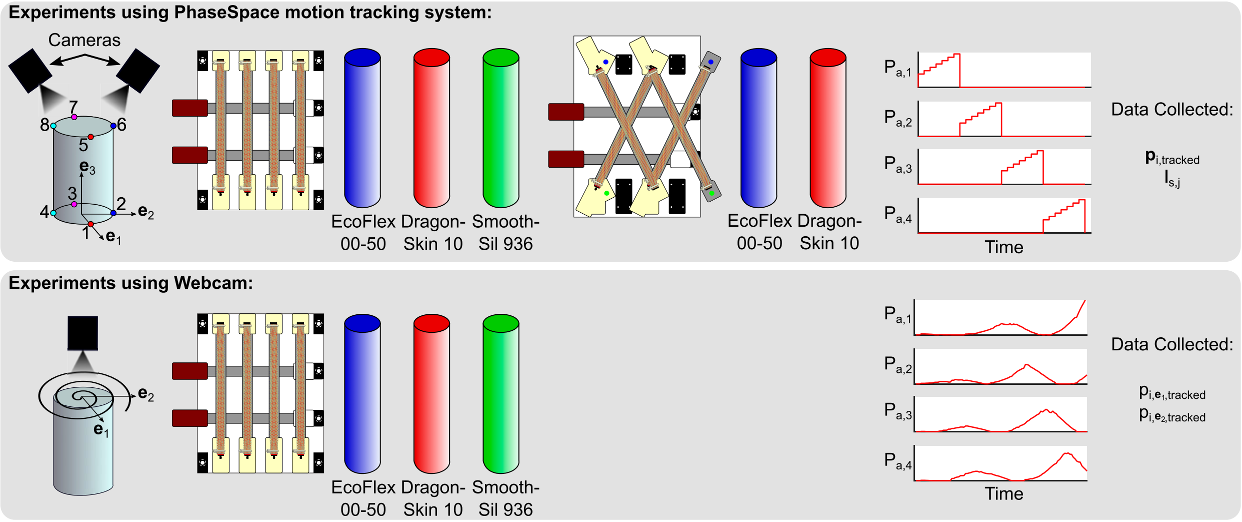

Figure 7. Experiments that were conducted, which used both a motion tracking system to track eight dots placed around the segment and a webcam to track movement along the $\mathbf{e}_1$–$\mathbf{e}_2$ plane. For the motion tracking experiments, the parallel skins were placed on all three material cylindrical structures while the twisting skins were only placed on the two softest segments. Each actuator was individually inflated to a variety of pressures and both the tracked point locations and the length of the sensors were recorded. The webcam experiments used only the Parallel Skin 1, which was placed on all three cylindrical structures. More complex pressure inputs were applied to the skin and the positions along the $\mathbf{e}_1$- and $\mathbf{e}_2$-axes were recorded.

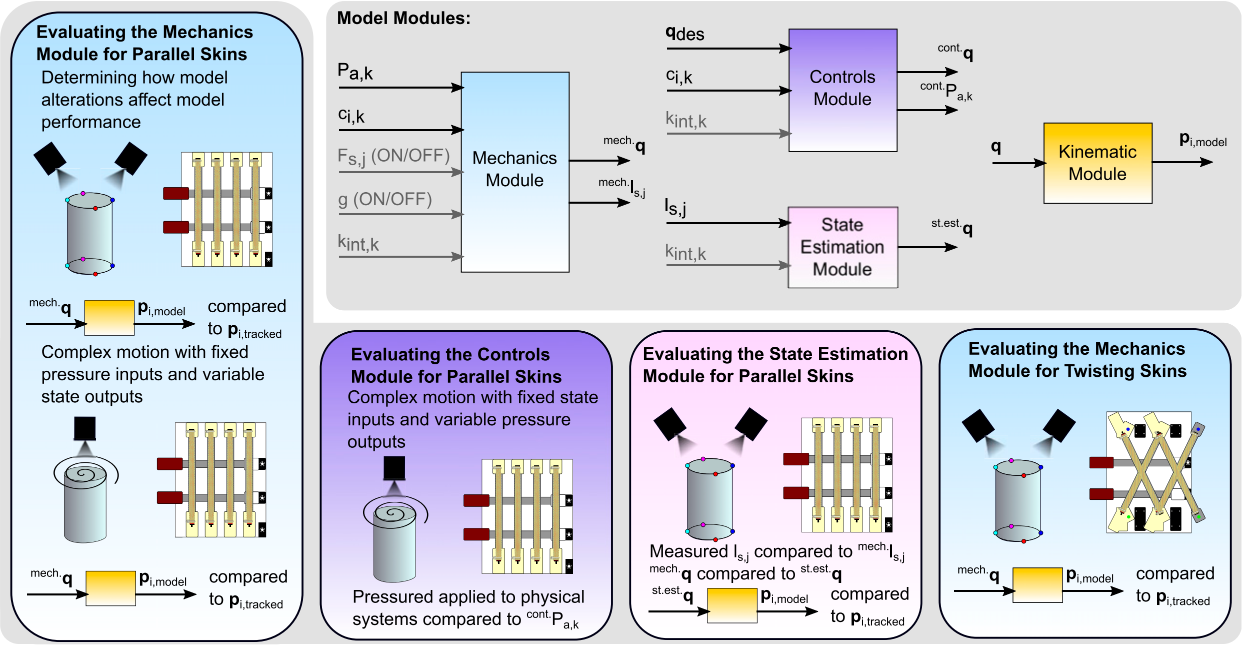

Figure 8. The top-right subfigure shows the modules. The parameters denoted in black exist for both our extended model as well as the previous model described in the Review of the Previous Model section. The gray parameters are new parameters for our extended model. Note that we only include parameters that are explored experimentally. The other subfigures explain which experimental data and skins were used in each analysis as well as a brief description of how that data was used.

Table 1. Full factorial study exploring how model features affect the accuracy of the model.

		Model Combination							
		C	C/G	C/F	C/I	C/G/F	C/G/I	C/F/I	C/G/F/I
New Model Effects	Compressibility	▨	▨	▨	▨	▨	▨	▨	▨
	Gravity		▨			▨	▨		▨
	Sensor Force			▨		▨		▨	▨
	Interface				▨		▨	▨	▨

includes all four model features. Figure 9(a) compares the results of the previous mechanics module, the C feature, and C/G/F/I combination to the collected motion tracking data for the Dragon Skin 10 segment when a single actuator is inflating. The previous model overshoots the deformation of the physical system at higher pressures while both variations of the new model have a reduction in the total deformation at higher pressures, which better matches the motion tracking data, highlighting the importance of including compressibility in the model. Figure 9(b) shows error that has been averaged for each pressure across all four actuators inflating (see equation (20)). The C feature and C/G/F/I combination outperform the previous model when the pressure in actuators is above 90 kPa. Both the C feature and C/G/F/I combination have an average error at or below 10% with a small improvement in performance for the C/G/F/I combination. Figure 9(c) shows a histogram of the errors for the tracked points across all pressures for all actuators which highlights the error distribution of the entire experiment. The error from the C/G/F/I combination is consistently below 10% with few readings reaching as high as 15%. The C feature has fewer errors below 5% than the C/G/F/I combination and a few errors reaching as high as 18%, but is also centered around 10%. The previous mechanics module, in comparison, has about 1/3 of the data points above 15% error. Thus, Figure 9(a)–(c) definitively shows the advantage of the expanded mechanics module over the previous mechanics module.

Table 2. Interface spring constants for all three segment materials for experiments listed in Table 1 that require interface springs for Parallel Skin 1. Note that C stands for compressibility, G stands for gravitational forces, F stands for sensor forces, and I stands for the interfaces to identify which model features were included in the model combinations.

			Model combination			
			C/I	C/F/I	C/G/I	C/G/F/I
Eco-Flex 00–50 (N/m)	Actuator	1	929	1947	58	338
		2	1171	1938	58	620
		3	794	1947	58	369
		4	928	1938	89	764
Dragon Skin 10 (N/m)	Actuator	1	545	1496	140	389
		2	590	1576	125	398
		3	1229	1683	356	819
		4	1090	1630	288	764
Smooth-Sil 936 (N/m)	Actuator	1	760	1228	500	800
		2	1066	1523	649	1063
		3	780	1166	461	777
		4	1208	1514	845	1232

Second, we demonstrate that the inclusion of each of the model features (i.e., compressibility, sensor and gravitational forces, and an interface between the skin and structure) improves the overall performance of the expanded model. We see a decrease in error for every additional feature with the best performance being the C/G/F/I combination, shown in Figure 9(d), with the exception of the C/G combination which showed a decrease in performance. This analysis demonstrates that there is an improvement in the overall performance by adding all of the features to the expanded model.

Finally, we show that the performance of the mechanics module is material-independent by performing the same analyses with the same parallel skin on cylindrical structures made from different materials (i.e., EcoFlex 00–50, Dragon Skin 10, and Smooth-Sil 936). All the segments showed comparable performance between the eight model combinations tested across multiple materials (see Figure 9(d)). This analysis was repeated for an additional Parallel Skin, which is shown in the Supplemental Materials (Section S8) and showed similar results. For the remainder of the paper, we elected to use the C/G/F/I combination of the mechanics module for our parallel skins.

4.1.2. Complex motions. To understand how the expanded mechanics module handles complex pressure patterns, we compared it against the tracked traces of the physical system captured by the webcam experiments.

In this analysis, we show the ability of the mechanics module to predict the behavior of systems following complex traces, both smooth circular traces and sharp corners. Figure 10 shows a comparison between the simulation and the physical experiment for all nine pattern and material combinations. The simulation traces similar shapes to the ones the physical system makes. The difference between the simulation and the physical system decreases as the elastic modulus of the material increases. We believe that the error seen in the EcoFlex 00–50 segment is due to the cylindrical structure buckling under the load from the skin leading to preferential bending in directions that were

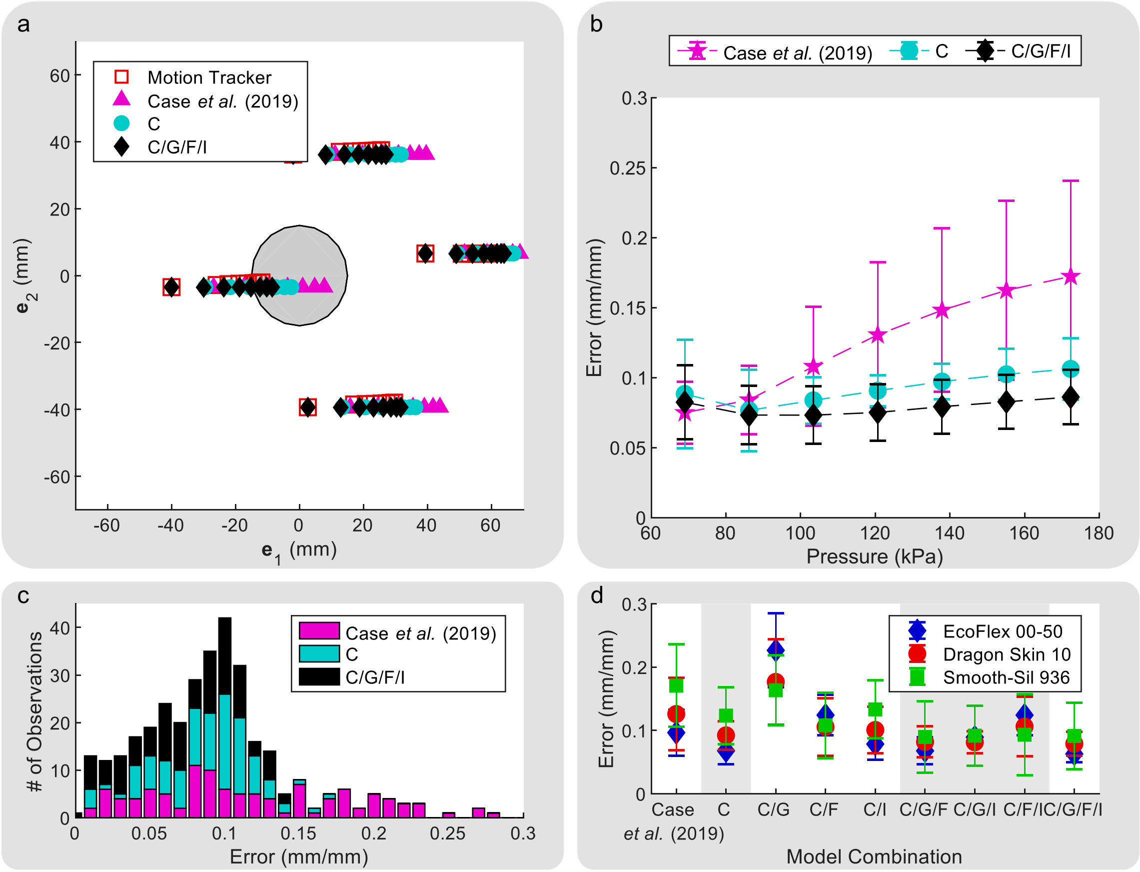

Figure 9. This figure demonstrates the differences between the previous mechanics module (Case et al., 2019) and the new mechanics module for Parallel Skin 1. (a) The top-down view of the Dragon Skin 10 segment as Actuator 1 is inflated showing the motion tracking markers compared to the previous mechanics module and the C and C/G/F/I model combinations. The light gray circle in the center represents the undeformed segment. (b) Comparison of the previous, C, and C/G/F/I model combinations' errors across the various pressures in all actuators for the Dragon Skin 10 segment. (c) A histogram showing the error between all the points and the previous, C, and C/G/F/I model combinations for all actuators inflating for the Dragon Skin 10 segment. (d) Comparison of each model error to the previous model for all segment materials. The light gray boxes in the background separate the number of components in each experiment. Note that C stands for compressibility, G stands for gravitational forces, F stands for sensor forces, and I stands for the interfaces to identify which model features were included in the model combinations.

not predicted by the simulation. We provide further discussion of how buckling should be considered during the design phase in the Supplemental Materials (Section S1). This analysis shows the ability of the mechanics model to predict behavior with complex pressure patterns across varying material stiffnesses.

4.2. Evaluating the performance of the controls module for parallel skins

To study the performance of the controls module, we put the measured states from the webcam experiments through both the extended and previous control modules. Their predicted pressures were then compared against the pressures used in the actual system.

In this analysis, we demonstrate that the expanded control module performs as well or better than the previous control module in pressure space. Figure 11 shows the controls modules' performances for the circular spiraling trace for all three cylindrical structure materials. Immediately, we can see that the previous controls module frequently drops the pressure to 0 kPa while the new controls module retains some pressure in the actuators throughout the spiral. This phenomenon is

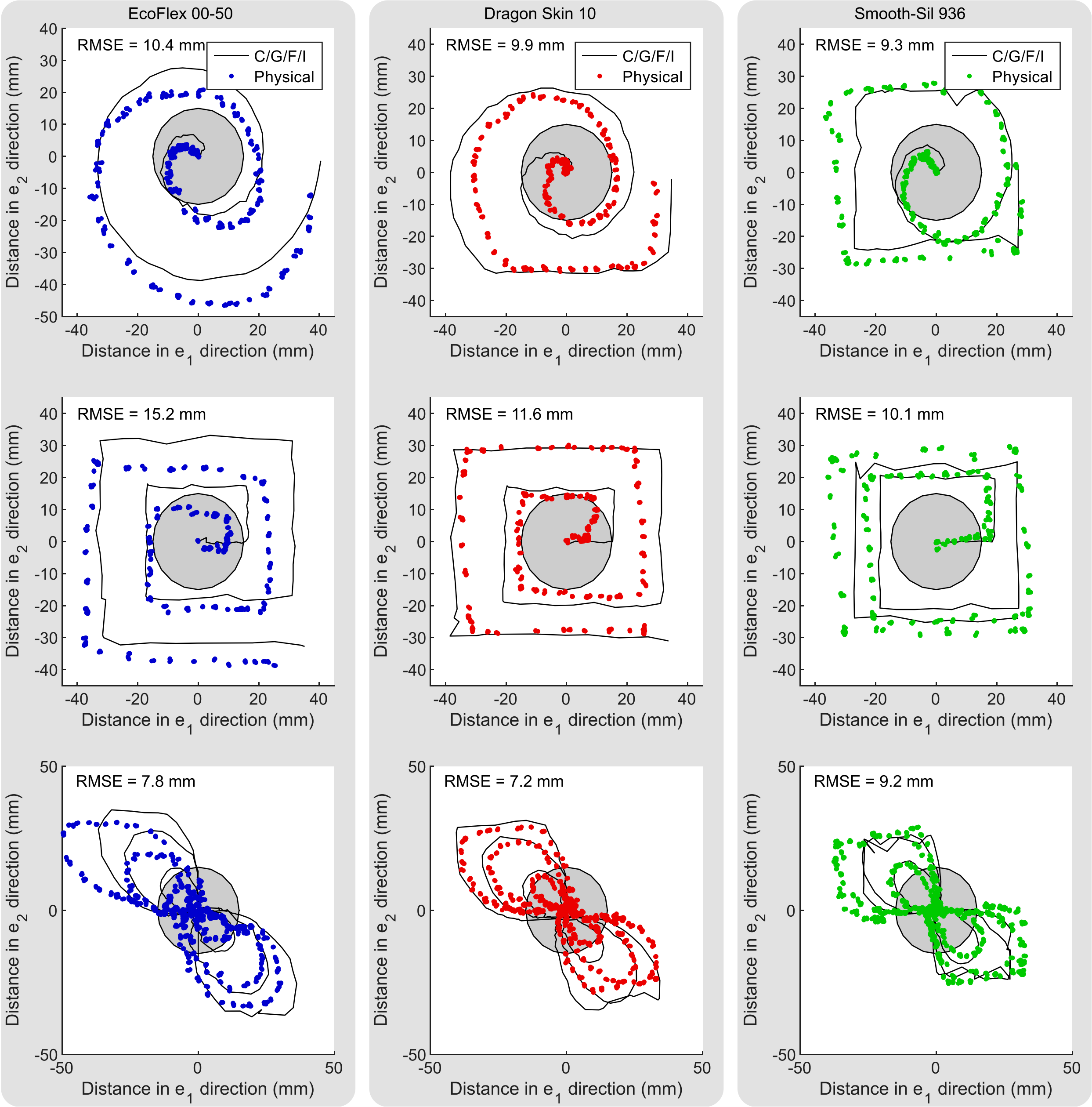

Figure 10. Comparison between the simulation and experimental performance for various pressure patterns on our EcoFlex 00–50, Dragon Skin 10, and Smooth-Sil 936 segments. Note that C stands for compressibility, G stands for gravitational forces, F stands for sensor forces, and I stands for the interfaces to identify which model features were included in the model combinations.

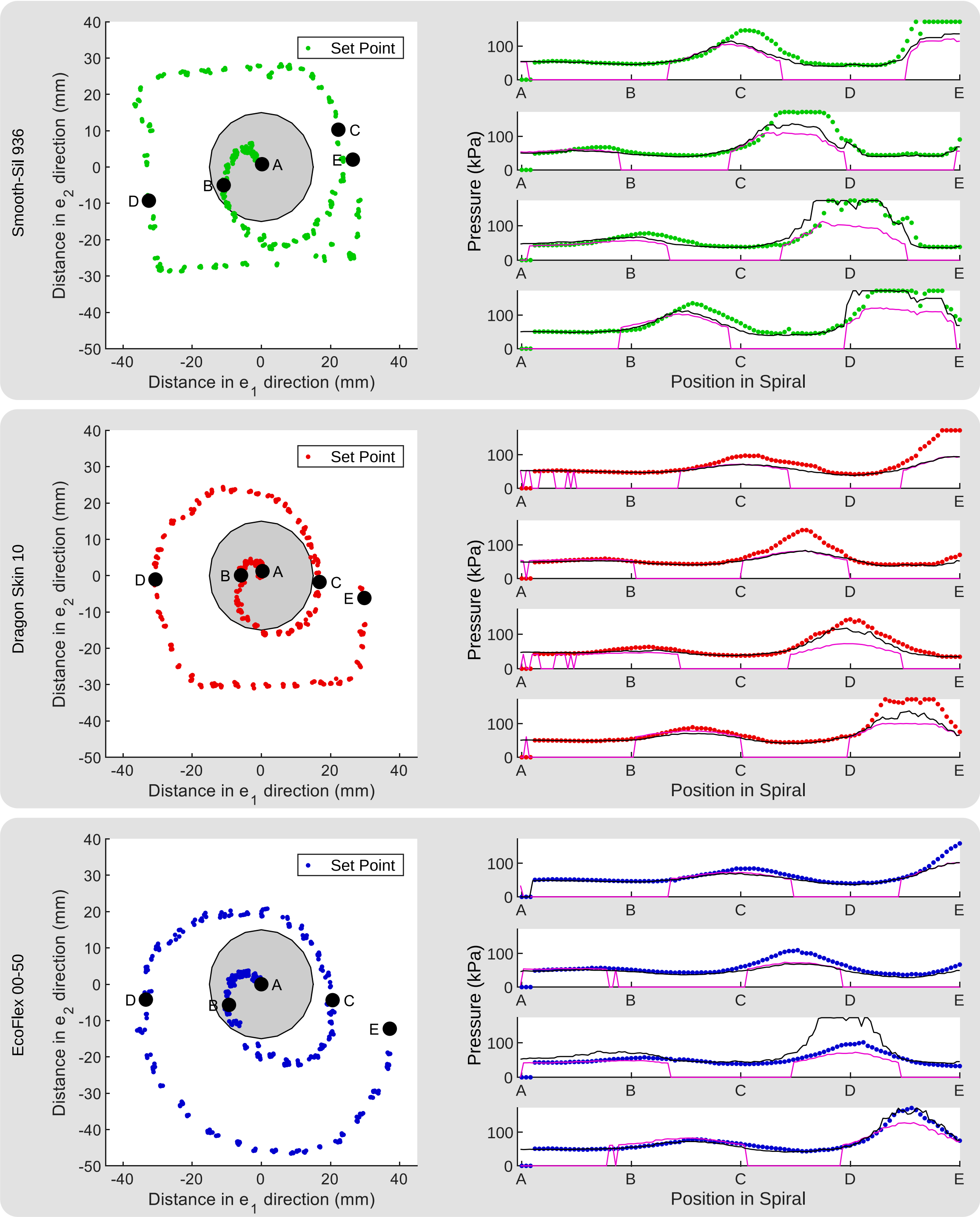

Figure 11. The controls module results for the circular spiral. For the images on the left, a top-down view provides the set points achieved by the physical system via generated pressure signals using a general robotic skin model. For plots on the right, the pressure in each actuator is shown with Actuator 1 at the top and Actuator 4 at the bottom. The left figures show the path taken by the structure corresponding to the material. The right figures show the pressures applied along the path. Key path points are identified by letters in all the graphs. In the right figures, the black lines are the actual pressure applied to the physical system, the magenta lines are the previous control module's (Case et al., 2019) predictions to achieve the desired set point, and the colored dotted lines are the new extended control module's predictions.

because the previous controls module forces only one actuator of the two antagonistic actuator pairs to be inflated at a time. The new controls module does not make this same assumption since it does not assume prior knowledge of actuator locations and has determined that there is no noticeable change to actuator force below 50 kPa. We can also see that the previous controls module predicts that it is able to reach locations

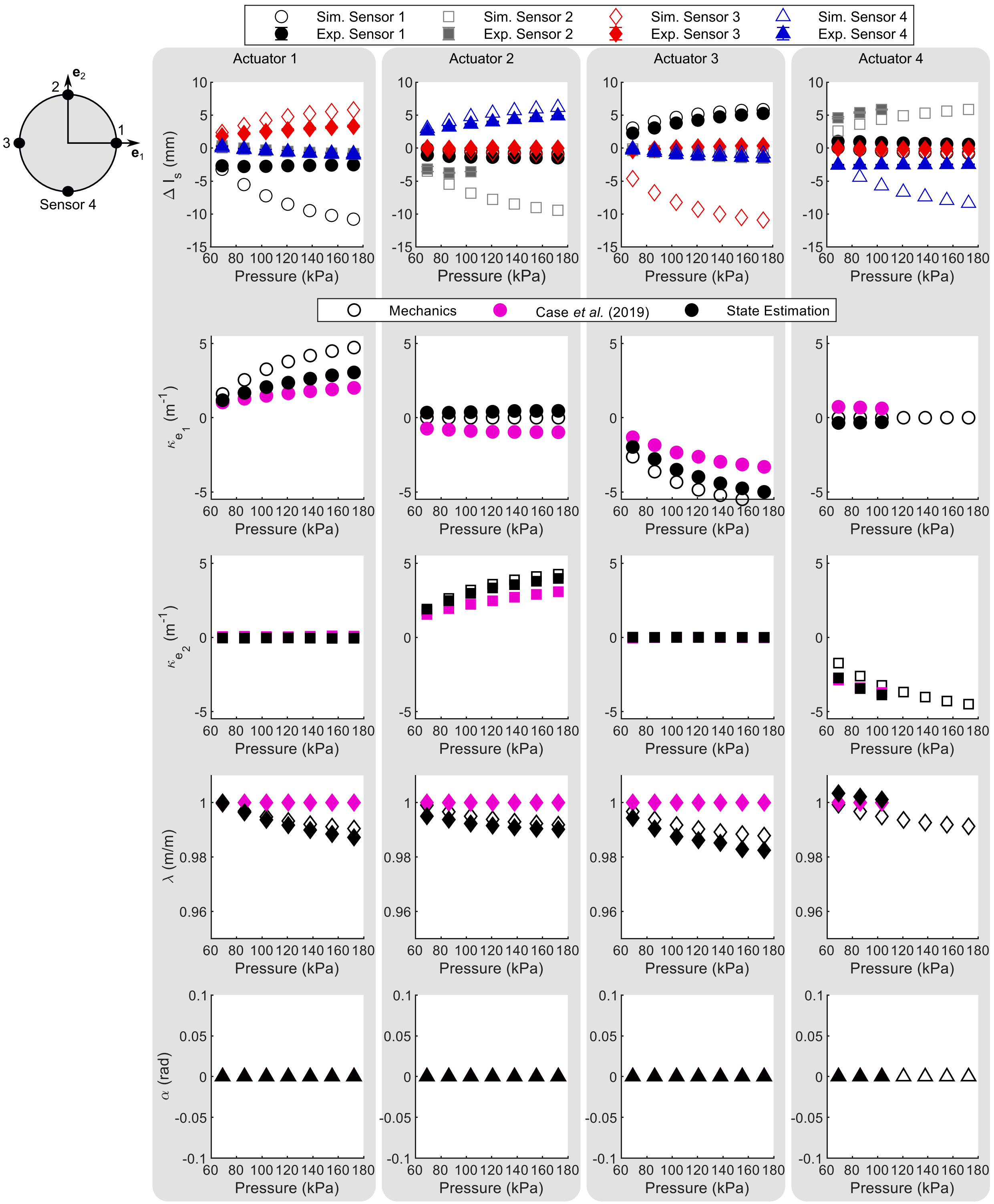

Figure 12. Comparing the sensor lengths and state estimation module to the mechanics module simulation for Parallel Skin 1 on the Dragon Skin 10 segment for Actuators 1–4. The top row of these graphs compares the experimental sensor lengths to the predicted sensor lengths from our simulation. The other four rows compare the predicted state from the previous state estimation module and the new state estimation module to the predicted state from the mechanics module.

that the new controls module is unable to reach (see point D for the Smooth-Sil 936 segment in Figure 11). This difference between the modules occurs because the previous controls module predicts a lower pressure to reach the location while the new controls module reaches the actuator limit, which matches what was actually applied to the system. The best predictions were on the cylindrical structure with the highest elastic

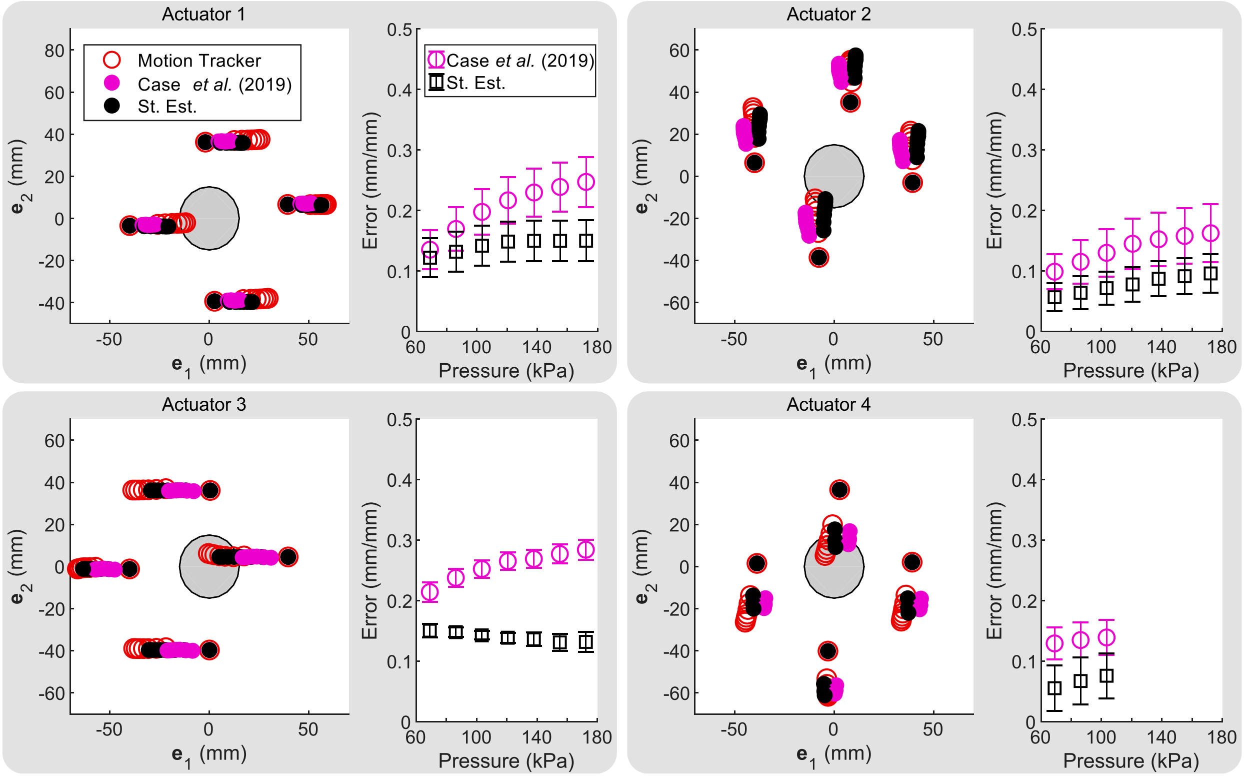

Figure 13. The state estimation results when the actuators were inflated on Parallel Skin 1 on a Dragon Skin 10 cylindrical structure. A comparison between the tracked positions, the previous state estimation module, and the new state estimation module, with the average error provided for each actuator.

modulus, decreasing as the material softens. These results were repeated for the other traces in the Supplemental Materials (Section S9).

4.3. Evaluating the performance of the state estimation module for parallel skins

To explore the state estimation performance, we used motion-tracking experiments. This study was divided into three analyses with the sensor data: (1) we compared the measured sensor lengths against the simulation predicted sensor lengths using the mechanics module, (2) we compared the states from our previous and new state estimation modules against the predicted state from our mechanics module, and (3) we compared the previous and new state estimation modules against the motion tracking data.

First, we demonstrate that the predicted sensor lengths from the expanded mechanics module are comparable to the measured lengths of the sensors and can be used to identify sensors that are providing insufficient data. This analysis is shown in the top row of Figure 12. From these graphs, we can see that the sensor underneath the active actuator is nonresponsive to changing strain, which may be due to the sensor experiencing pressure from the active actuator, while the sensor opposite of the active actuator does respond similarly to the predicted length. The other two sensors followed their predicted trends (i.e., decreasing length with increasing pressure) well, which confirms that compression was an important component missing from the previous model (Case et al., 2019). Comparing the measured sensor lengths against the predicted sensor lengths of the mechanics model provides insight into how the sensor placement is working on the physical system.

Second, we demonstrate that the predicted state from the expanded state estimation module better matches the predicted state from the expanded mechanics module than the previous state estimation module. The bottom four rows of graphs in Figure 12 compare the results of the state estimation models against the predicted states of the mechanics module. The state estimation modules were only provided with sensor lengths that were meaningful. In some cases (see Actuator 4 in Figure 12), there was insufficient sensor data to get an estimated state for all pressures. Figure 12 shows that the new state estimation module appears as if it will perform better than the previous state estimation module when compared to physical results given the previously established accuracy of the mechanics module.

Finally, we demonstrate that the expanded state estimation module does outperform the previous state estimation module when compared to a physical system (specifically the motion tracking data). Figure 13 shows a

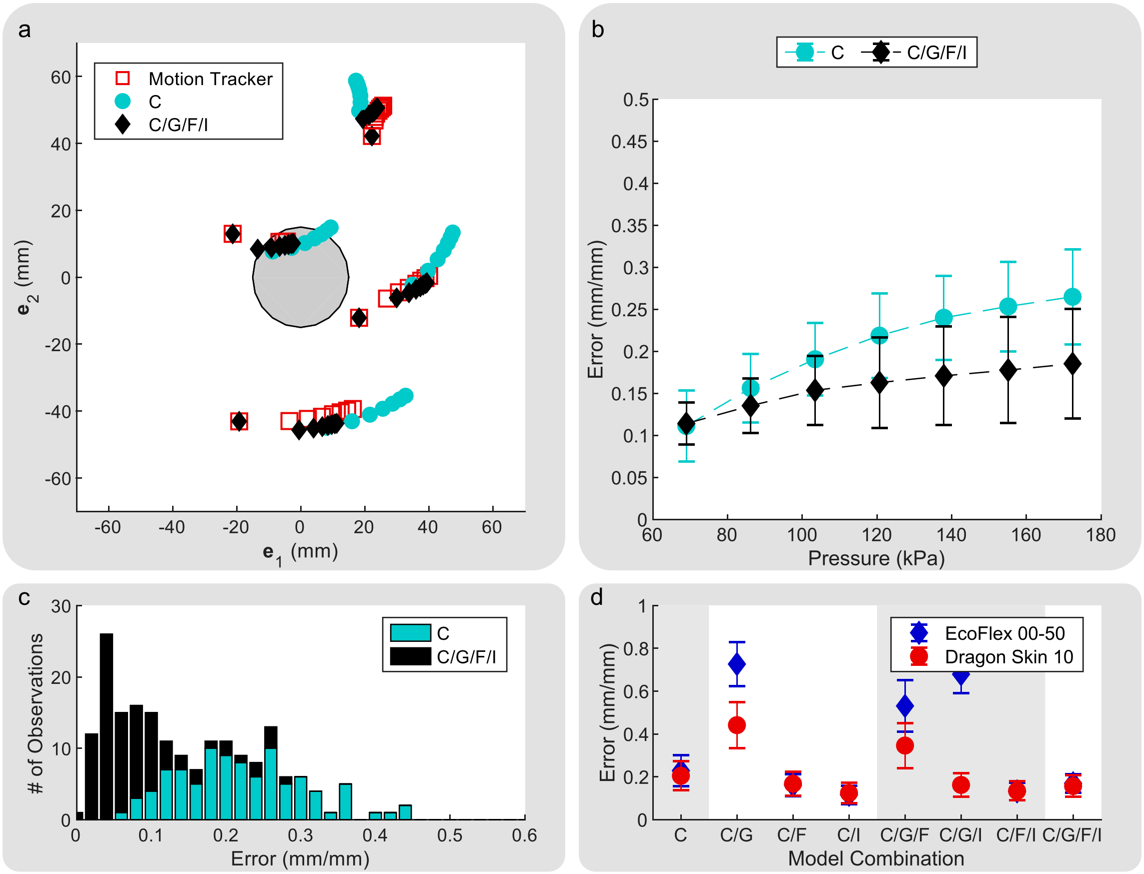

Figure 14. This figure demonstrates the differences between the changes made to the mechanics module and for Twisting Skin 1. (a) The top-down view of the Dragon Skin 10 segment as Actuator 1 is inflated showing the motion tracking markers compared to the C and C/G/F/I models. The light gray circle in the center represents the undeformed segment. (b) Comparison of the C and C/G/F/I feature/combination errors across the various pressures in all actuators. (c) A histogram showing the error between all the points and the C and C/G/F/I feature/combination models for all actuators for the Dragon Skin 10 segment. (d) Comparison of each combination error for all segment materials. The light gray boxes in the background separate the number of components in each experiment. Note that C stands for compressibility, G stands for gravitational forces, F stands for sensor forces, and I stands for the interfaces to identify which model features were included in the model combinations.

comparison between the motion tracking points and the predicted location of those points for the previous and new state estimation modules for each actuator inflating on the Dragon Skin 10 segment. The error between the state estimation modules and the motion tracking points is also provided. Figure 13 shows that the error for the new module falls under 15% and the error for the previous module reaches a maximum of about 30%. The results are repeated for the EcoFlex 00–50 and Smooth-Sil 936 structures in the Supplemental Materials (Section S10). The error for the EcoFlex 00–50 segment is slightly higher overall while the error for the Smooth-Sil 936 segment is slightly lower matching the error trends we have seen in previous studies.

4.4. Evaluating the performance of the mechanics module for twisting skins

To study the performance of the mechanics module on alternative skin designs, we applied the same approach described in the Introduction of Model Features section to our twisting skins. For the twisting skin, we found the maximum lengths traveled were 74 and 66 mm for EcoFlex 00–50 and Dragon Skin 10, respectively.

First, we demonstrate that the extended mechanics module is able to approximate the response of the physical system. For this analysis, we compared the performance of the mechanics model using the C feature and C/G/F/I combination described in Table 1 against the performance of the physical system when a single actuator is inflating on Twisting Skin 1, shown in Figure 14(a). The C feature appears to twist more than the physical system while the C/G/F/I combination does not twist enough for one of the points. This overtwisting could be occurring because the torsional stiffness is too low, which could be due to an error in the assumed Poisson's ratio. The unique factor that affects torsional stiffness, but not axial or bending stiffness, is Poisson's ratio. Elastomers are generally assumed to be incompressible, but if the material is not truly incompressible, we will see an increase in torsional stiffness which will

Table 3. Interface spring constants for all three segment materials for experiments listed in Table 1 that require interface springs for Twisting Skin 1. Note that C stands for compressibility, G stands for gravitational forces, F stands for sensor forces, and I Stands for the interfaces to identify which model features were included in the model combinations.

			Model combination			
			C/I	C/F/I	C/G/I	C/G/F/I
Eco-Flex 00–50 (N/m)	Actuator	1	143	486	500	96
		2	127	527	500	96
		3	171	598	500	86
		4	95	354	500	86
Dragon Skin 10 (N/m)	Actuator	1	230	549	70	193
		2	117	352	21	111
		3	241	563	77	215
		4	85	206	27	82

reduce twisting. Further research into the material properties of elastomers is required to understand if this is the cause of the error seen here. However, the spring interface present in the C/G/F/I combination is able to compensate for the error to provide an approximation of the system. Figure 14(b) shows that while the average error for both the C feature and C/G/F/I combination start approximately the same, the overtwisting of the C feature quickly causes an increase in average error. The difference between the behavior of the two models is further highlighted in Figure 14(c), which shows that the error of the C/G/F/I combination is skewed heavily below 10%. Meanwhile, the error in the C feature is skewed slightly higher with substantially fewer values below 10% and some points getting as high as 46% error. Thus, although the error is not as low as the error for parallel skins, the mechanics module is able to capture the complex behavior of the twisting skins.

Second, we demonstrate that the inclusion of the model features, especially the interface, to the expanded mechanics module improves performance. Figure 14(d) shows the performance of each model combination as features are added to the system and Table 3 contains the spring constants for each combination. Here, we see that the gravitational force worsens the performance. We can also note that the C/G/F combination performs worse than either the C/F or C/I combination, which indicates that the gravitational force is causing too much deformation. This large error due to gravitational force is likely exacerbated by the overtwisting seen in combinations without the interface. This analysis shows that the benefits of including the model features in the mechanics module extend to twisting skins as well, although additional considerations are needed to improve performance.

Finally, we show that the performance of the mechanics module is material-independent for twisting skins by performing the same test on multiple materials. Figure 14(d) shows that both the EcoFlex 00–50 and Dragon Skin 10 cylindrical structures follow the same basic trends with the exception of the C/G/I combination. For the soft EcoFlex 00–50 cylindrical structure, this combination struggled to find valid solutions to the deformation within the limitations given for the optimization. These results were repeated for an additional Twisting Skin provided in the Supplemental Materials (Section S11). With proper calibration, the mechanics module is able to approximate the performance of robotic skins wrapped around various materials and with varying actuator placement.

5. Conclusion

In this paper, we extended quasi-static models for robotic skins wrapped around soft cylindrical structures by adding compressibility, gravitational forces, sensor forces (which required the development of a sensor model that incorporated plastic deformation), and a skin-structure interface (which took the form of a spring at attachment points between the structure and skin). We showed that the expanded mechanics, controls, and state estimation modules outperformed the previous model for robotic skins with a parallel component layout. The expanded mechanics module maintained overall accuracy in performance across multiple host (cylinder) materials and with varying pressure inputs while the controls and state estimation models increased in accuracy as the stiffness of materials increased. We also showed that the mechanics module can reasonably predict the behavior of robotic skins with more generalized actuator placement.

In the future, we would like to adapt this model further to create a design tool for designing robotic skins. To accomplish that goal, we would need to remove the empirically derived parameters for the actuators and the interface between the skin and the underlying structure. While there is existing research on the theoretical modeling of McKibben actuators (Chou and Hannaford, 1996; Davis et al., 2003; Bishop-Moser and Kota, 2015), further work is required to understand the physics between the skin and underlying structure. Additionally, an understanding of how the sensors and actuators interact with each other could assist in designing sensor and actuator placements. Having a design tool would be able to save both time and material in creating new skin designs. Improvements in the optimization of this model could enable its use in real-time control for future applications such that the state estimation model could assist feedback controllers and the control model could serve as a feedforward model.

This new model, along with future design tools and robotic skins technology, can revolutionize human–robot interaction. Beyond resource-limited environments, where robotic skins can be reused for various functions with the same hardware, they hold promise for healthcare, rehabilitation, and daily assistance for users with disabilities or posture issues. By controlling inert objects from their surface, the potential for wearables and assistive devices is vast. This model aims to enhance system predictability to tackle these grand challenges.

Declaration of conflicting interests

The author(s) declared no potential conflicts of interest with respect to the research, authorship, and/or publication of this article.

Funding

The author(s) disclosed receipt of the following financial support for the research, authorship, and/or publication of this article: J.C.C. was supported by a NASA Space Technology Research Fellowship (NNX15AQ75H) and an NRC Research Associateship award at NIST. S.J.W. was supported by a NASA NSTGRO Fellowship (80NSSC22K1188). R.K.B. was supported by the National Science Foundation under award IIS-1954591.

ORCID iDs

Jennifer C Case https://orcid.org/0000-0003-3264-0558
Stephanie J Woodman https://orcid.org/0000-0003-4858-6226
Rebecca Kramer-Bottiglio https://orcid.org/0000-0003-2324-8124

Supplemental Material

Supplemental material for this article is available online.

Note

1. Certain commercial materials and equipment are mentioned in this paper to specify the experiment adequately. Such identification is not intended to imply recommendation or endorsement by the National Institute of Standards and Technology, nor does it imply that the material is necessarily the best available for the purpose.

References

Almanzor E, Ye F, Shi J, et al. (2023) Static shape control of soft continuum robots using deep visual inverse kinematic models. *IEEE Transactions on Robotics*.

Armanini C, Boyer F, Mathew AT, et al. (2023) Soft robots modeling: a structured overview. *IEEE Transactions on Robotics* 39(3): 1728–1748.

Bishop-Moser J and Kota S (2015) Design and modeling of generalized fiber-reinforced pneumatic soft actuators. *IEEE Transactions on Robotics* 31(3): 536–545. DOI: 10.1109/TRO.2015.2409452.

Booth JW, Shah D, Case JC, et al. (2018) OmniSkins: robotic skins that turn inanimate objects into multifunctional robots. *Science Robotics* 3(22): eaat1853. DOI: 10.1126/scirobotics.aat1853. https://robotics.sciencemag.org/content/3/22/eaat1853.

Burgner-Kahrs J, Rucker DC and Choset H (2015) Continuum robots for medical applications: a survey. *IEEE Transactions on Robotics* 31(6): 1261–1280. DOI: 10.1109/TRO.2015.2489500.

Camarillo D, Milne C, Carlson C, et al. (2008) Mechanics modeling of tendon-driven continuum manipulators. *IEEE Transactions on Robotics* 24(6): 1262–1273. DOI: 10.1109/TRO.2008.2002311.

Campisano F, Ozel S, Ramakrishnan A, et al. (2017) Towards a soft robotic skin for autonomous tissue palpation. In: 2017 IEEE international conference on robotics and automation (ICRA), Singapore, 29 May 2017–03 June 2017, pp. 6150–6155. DOI: 10.1109/ICRA.2017.7989729.

Case JC, Booth J, Shah DS, et al. (2018) State and stiffness estimation using robotic fabrics. In: 2018 IEEE international conference on soft robotics (RoboSoft), Livorno, Italy, 24–28 April 2018, pp. 522–527. DOI: 10.1109/ROBOSOFT.2018.8405379.

Case JC, Yuen MC, Jacobs J, et al. (2019) Robotic skins that learn to control passive structures. *IEEE Robotics and Automation Letters* 4(3): 2485–2492. DOI: 10.1109/LRA.2019.2906552.

Case JC, Gibert J, Booth J, et al. (2020) Spinal helical actuation patterns for locomotion in soft robots. *IEEE Robotics and Automation Letters*, 1. DOI: 10.1109/LRA.2020.2982352. Conference Name: IEEE Robotics and Automation Letters.

Chossat JB, Tao Y, Duchaine V, et al. (2015) Wearable soft artificial skin for hand motion detection with embedded microfluidic strain sensing. In: 2015 IEEE international conference on robotics and automation (ICRA), Seattle, WA, USA, 26–30 May 2015, pp. 2568–2573. DOI: 10.1109/ICRA.2015.7139544.

Chou CP and Hannaford B (1996) Measurement and modeling of McKibben pneumatic artificial muscles. *IEEE Transactions on Robotics and Automation* 12(1): 90–102. DOI: 10.1109/70.481753.

Davis S, Tsagarakis N, Canderle J, et al. (2003) Enhanced modelling and performance in braided pneumatic muscle actuators. *The International Journal of Robotics Research* 22(3): 213–227. DOI: 10.1177/0278364903022003006.

Della Santina C, Duriez C and Rus D (2023) Model-based control of soft robots: a survey of the state of the art and open challenges. *IEEE Control Systems Magazine* 43(3): 30–65.

Faulkner J and Dirven S (2017) A generalised, modular, approach for the forward kinematics of continuum soft robots with sections of constant curvature. In: 2017 24th international conference on mechatronics and machine vision in practice (M2VIP), Auckland, New Zealand, 21–23 November 2017, pp. 1–6. DOI: 10.1109/M2VIP.2017.8211510.

Guo J, Xiang C, Conn A, et al. (2020) All-soft skin-like structures for robotic locomotion and transportation. *Soft Robotics* 7(3): 309–320. DOI: 10.1089/soro.2019.0059. https://www.ncbi.nlm.nih.gov/pmc/articles/PMC7301317/.

Heng W, Yang G, Pang G, et al. (2021) Fluid-driven soft CoboSkin for safer human–robot collaboration: fabrication and adaptation. *Advanced Intelligent Systems* 3(3): 2000038. DOI:10.1002/aisy.202000038. https://onlinelibrary.wiley.com/doi/pdf/10.1002/aisy.202000038.

Hughes D, Lammie J and Correll N (2018) A robotic skin for collision avoidance and affective touch recognition. *IEEE Robotics and Automation Letters* 3(3): 1386–1393. DOI:10.1109/LRA.2018.2799743.

Hwang ES, Seo JH and Kim YJ (2007) A polymer-based flexible tactile sensor for both normal and shear load detections and its application for robotics. *Journal of Microelectromechanical Systems* 16(3): 556–563. DOI: 10.1109/JMEMS.2007.896716.

Koo IM, Jung K, Koo JC, et al. (2008) Development of soft-actuator-based wearable tactile display. *IEEE Transactions on Robotics* 24(3): 549–558. DOI: 10.1109/TRO.2008.921561.

Koo JH, Lee YJ, Kim HJ, et al. (2024) Electronic skin: opportunities and challenges in convergence with machine learning. *Annual Review of Biomedical Engineering* 26(1): 331–355. DOI: 10.1146/ANNUREV-BIOENG-103122-032652/CITE/REFWORKS. https://www.annualreviews.org/content/journals/10.1146/annurev-bioeng-103122-032652.

Larson C, Peele B, Li S, et al. (2016) Highly stretchable electroluminescent skin for optical signaling and tactile sensing. *Science* 351(6277): 1071–1074. DOI: 10.1126/science.aac5082. https://science.sciencemag.org/content/351/6277/1071.

Lipomi DJ, Vosgueritchian M, Tee BCK, et al. (2011) Skin-like pressure and strain sensors based on transparent elastic films of carbon nanotubes. *Nature Nanotechnology* 6(12): 788–792. DOI: 10.1038/nnano.2011.184. https://www.nature.com/nnano/journal/v6/n12/abs/nnano.2011.184.html.

Lv X, Liu Y, Yu J, et al. (2022) Smart fibers for self-powered electronic skins. *Advanced Fiber Materials* 5(2): 401–428. DOI: 10.1007/S42765-022-00236-6. https://link.springer.com/article/10.1007/s42765-022-00236-6.

Mehringer A, Kandhari A, Chiel H, et al. (2017) An integrated compliant fabric skin softens, lightens, and simplifies a mesh robot. In: *Biomimetic and Biohybrid Systems, Lecture Notes in Computer Science*. Cham: Springer, 315–327. DOI: 10.1007/978-3-319-63537-8_27. https://link.springer.com/chapter/10.1007/978-3-319-63537-8_27.

Mullins L (1948) Effect of stretching on the properties of rubber. *Rubber Chemistry and Technology* 21(2): 281–300.

Ogden RW and Ogden RW (2003) Nonlinear elasticity with application to material modelling. https://rcin.org.pl/ippt/publication/24849.

O'Neill J, Lu J, Dockter R, et al. (2018) Stretchable, flexible, scalable smart skin sensors for robotic position and force estimation. *Sensors* 18(4): 953. DOI: 10.3390/s18040953. https://www.mdpi.com/1424-8220/18/4/953.

Renda F, Cianchetti M, Giorelli M, et al. (2012) A 3d steady-state model of a tendon-driven continuum soft manipulator inspired by the octopus arm. *Bioinspiration & Biomimetics* 7(2): 025006. DOI: 10.1088/1748-3182/7/2/025006. https://doi.org/10.1088%2F1748-3182%2F7%2F2%2F025006. Publisher: IOP -Publishing.

Renda F, Cacucciolo V, Dias J, et al. (2016) Discrete cosserat approach for soft robot dynamics: a new piece-wise constant strain model with torsion and shears. In: 2016 IEEE/RSJ international conference on intelligent robots and systems (IROS), Daejeon, Korea (South), 09–14 October 2016, pp. 5495–5502. DOI: 10.1109/IROS.2016.7759808.

Roberts P, Zadan M and Majidi C (2021) Soft tactile sensing skins for robotics. *Current Robotics Reports* 2(3): 343–354. DOI: 10.1007/S43154-021-00065-2. https://link.springer.com/article/10.1007/s43154-021-00065-2.

Rucker DC and Webster RJ (2014) Mechanics of continuum robots with external loading and general tendon routing. In: *Experimental Robotics, Springer Tracts in Advanced Robotics*. Berlin, Heidelberg: Springer, 645–654. DOI: 10.1007/978-3-642-28572-1_44. https://link-springer-com.ezproxy.lib.purdue.edu/chapter/10.1007/978-3-642-28572-1_44.

Russo M, Sadati SMH, Dong X, et al. (2023) Continuum robots: an overview. *Advanced Intelligent Systems* 5(5): 2200367.

Shah DS, Yang EJ, Yuen MC, et al. (2021) Jamming skins that control system rigidity from the surface. *Advanced Functional Materials* 31(1): 2006915.

Shah D, Woodman SJ, Sanchez-Botero L, et al. (2023a) Stretchable shape-sensing sheets. *Advanced Intelligent Systems* 5(12): 2300343.

Shah DS, Woodman SJ, Buckner TL, et al. (2023b) Robotic skins with integrated actuation, sensing, and variable stiffness. *IEEE Robotics and Automation Letters*.

Sharma S, Pradhan GB, Jeong S, et al. (2023) Stretchable and all-directional strain-insensitive electronic glove for robotic skins and human-machine interfacing. *ACS Nano* 17(9): 8355–8366. DOI: 10.1021/ACSNANO.2C12784. https://pubs.acs.org/doi/full/10.1021/acsnano.2c12784.

Shih B, Shah D, Li J, et al. (2020) Electronic skins and machine learning for intelligent soft robots. *Science Robotics* 5(41): eaaz9239. DOI: 10.1126/scirobotics.aaz9239. https://robotics.sciencemag.org/content/5/41/eaaz9239.Publisher:ScienceRoboticsSection:Review.

Shu S, Wang Z, Chen P, et al. (2023) Machine-learning assisted electronic skins capable of proprioception and exteroception in soft robotics. *Advanced Materials* 35(18): 2211385. DOI: 10.1002/ADMA.202211385. https://onlinelibrary.wiley.com/doi/10.1002/adma.202211385.

Soter G, Garrad M, Conn AT, et al. (2019) Skinflow: a soft robotic skin based on fluidic transmission. In: 2019 2nd IEEE International Conference on Soft Robotics (RoboSoft), Seoul, Korea (South), 14–18 April 2019, pp. 355–360. DOI: 10.1109/ROBOSOFT.2019.8722744.

Steltz E, Mozeika A, Rodenberg N, et al. (2009) JSEL: jamming skin enabled locomotion. In: IEEE/RSJ international conference on intelligent robots and systems, St. Louis, MO, USA, 10–15 October 2009, pp. 5672–5677. DOI: 10.1109/IROS.2009.5354790.

Teyssier M, Parilusyan B, Roudaut A, et al. (2021) Human-like artificial skin sensor for physical human-robot interaction. In: 2021 IEEE international conference on robotics and automation (ICRA), Xi'an, China, 30 May 2021–05 June 2021, pp. 3626–3633. DOI: 10.1109/ICRA48506.2021.9561152.

Tummers M, Lebastard V, Boyer F, et al. (2023) Cosserat rod modeling of continuum robots from Newtonian and Lagrangian perspectives. *IEEE Transactions on Robotics*.

Webster RJ and Jones BA (2010) Design and kinematic modeling of constant curvature continuum robots: a review. *The*

International Journal of Robotics Research 29: 1661–1683. DOI: 10.1177/0278364910368147. https://ijr.sagepub.com/content/early/2010/06/09/0278364910368147.

White EL, Yuen MC, Case JC, et al. (2017) Low-cost, facile, and scalable manufacturing of capacitive sensors for soft systems. *Advanced Materials Technologies* 2(9): 1700072. DOI: 10.1002/admt.201700072.

Yan H, Wang Y, Shen W, et al. (2022) Cable-driven continuum robot perception using skin-like hydrogel sensors. *Advanced Functional Materials* 32(34): 2203241. DOI: 10.1002/adfm.202203241. https://onlinelibrary.wiley.com/doi/abs/10.1002/adfm.202203241._eprint.

Zhang J, Fang Q, Xiang P, et al. (2022) A survey on design, actuation, modeling, and control of continuum robot. *Cyborg and Bionic Systems*.

Zhu M, Do TN, Hawkes E, et al. (2020) Fluidic fabric muscle sheets for wearable and soft robotics. *Soft Robotics* 7(2): 179–197. DOI: 10.1089/soro.2019.0033. https://www.liebertpub.com/doi/abs/10.1089/soro.2019.0033. Publisher: MaryAnnLiebert, Inc., Publishers.